Research article

Compact-porous hole-transport-layer for highly efficient near-infrared region transparent perovskite solar cells for tandem applications

Barkha Tyagi [a], Neetesh Kumar [a], Hock Beng Lee [a], Young Min Song [b], Sinyoung Cho [c], Jong-Soo Lee [c], Jae-Wook Kang [a],[*]

[a] Department of Flexible and Printable Electronics, LANL-JBNU Engineering Institute-Korea, Jeonbuk National University, Jeonju 54896, Republic of Korea
[b] School of Electrical Engineering and Computer Science, Gwangju Institute of Science and Technology, 123 Cheomdangwagi-ro, Buk-gu, Gwangju 61005, Republic of Korea
[c] Department of Energy Science and Engineering, DGIST, Daegu 42988, Republic of Korea

ARTICLE INFO

ABSTRACT

Wide-bandgap perovskites solar cells (PSCs) are vital as top cells in perovskite-based tandem solar cells (TSCs). However, poor band alignment with the charge transport layer and unwanted parasitic absorption in the top semitransparent-PSC (ST-PSC) are major factors limiting the power conversion efficiency (PCE) of TSCs. Herein, we present a compact-porous nickel oxide (cp-NiO$_x$) hole-transport layer (HTL) sequentially fabricated using a sol-gel suspension and colloidal suspension of highly crystalline NiO$_x$. The cp-NiO$_x$ film exhibited enhanced transparency, mesoporous surface morphology, and better energy band alignment with a 1.68 eV perovskite film for fabricating highly near-infrared transparent (∼92 % (@800–1200 nm)) ST-PSCs. The best cell achieved a PCE of 15.9 %. In addition, a four-terminal perovskite/silicon TSC based on the cp-NiO$_x$ HTL achieved an outstanding PCE of ∼26.0 %. The tailored energy band structure and reduced parasitic absorption in the near-infrared region of the ST-PSCs based on the cp-NiO$_x$ HTL enabled fabrication of highly efficient inverted ST-PSCs for perovskite/silicon TSCs.

© 2023 Elsevier B.V. All rights reserved.

1. Introduction

Silicon solar cells (SiSCs) are the mainstream technology of photovoltaics with a recent record power conversion efficiency (PCE) of ∼26.81% by LONGI, which is very close to the Shockley-Queisser (S-Q) limit [1,2]. To date, achieving a PCE that can surpass the S-Q limit has not been viable in a single junction solar cell due to the absorption loss below the bandgap. To overcome this efficiency limit, tandem solar cell (TSC) structures have been considered a promising strategy. The simplest form of a tandem configuration is the integration of a wide-band-gap top cell with a narrow-band-gap bottom cell. The TSC structure allows high-energy photon to be harvested by the top-cell and allows the bottom cell to harvest the transmitted low-energy-photons. These tandem configurations require a highly near-infrared (NIR) transparent top cell. Organic-inorganic halide-based perovskite materials offer excellent band-gap

tunability which makes them ideal top cell candidates for tandem configurations [3–5]. Perovskite solar cells (PSCs) having an inverted structure offer excellent PCE and, device stability [6]. The inorganic hole-transport layer (HTL) in inverted PSCs is the key for high device stability. Herein, nickel oxide (NiO$_x$) shows tremendous potential due to its low-cost, high hole mobility, energy bands well aligned with the perovskite layer, and superior stability [7]. Moreover, PSCs based on NiO$_x$ exhibited higher transmittance in the NIR region compared to PSCs consisting organic HTLs such as PEDOT:PSS and PTAA that makes them promising candidates for fabricating semitransparent-PSCs (ST-PSCs) for perovskite/silicon TSC applications [8].

Several reports demonstrated deposition of NiO$_x$ films for PSC application using different solution and non-solution-based techniques possessing distinct morphologies, such as compact morphologies using the combustion [9], sputtering [10], and spray pyrolysis techniques [11] and nanostructured NiO morphologies using the conventional sol-gel [12], nanoparticle [13], and pulsed laser deposition techniques [14]. However, most of the PSCs based on solution processed NiO$_x$ HTLs yielded lower device performance than

expected and exhibited a particularly low open-circuit voltage (V_{OC}). The low V_{OC} of the PSCs could be ascribed to the existence of interstitial defects on the surface of the NiO$_x$ films [15,16]. To realize highly efficient and stable ST-PSCs for perovskite/silicon TSCs, we need highly efficient NiO$_x$ HTL, which can yield a higher V_{OC}. In general, solution processed NiO$_x$ suffers from poor surface morphologies and mismatched band alignment with the perovskite layer, which causes Voc loss in PSCs. Incorporating metals into the NiO$_x$ material can allow tuning of band-alignment, resulting in better hole extraction efficiency. Conversely, these metal dopants can cause parasitic optical absorption in ST-PSCs leading to transmittance losses over wide spectral ranges causing photocurrent loss in the bottom cell in TSC [17]. Therefore, further research is required to develop an efficient NiO$_x$ HTL for ST-PSCs that can yield high PCEs as top cells and provide high NIR transmittance for bottom SiSC in TSCs. Several strategies have been adopted to minimize the optical losses in ST-PSCs; however, the ideal transparency to efficiency trade-off is far from being achieved [18–20]. One such strategy to overcome the conductivity issues and voltage loss in PSCs without doping the charge-transport layer (CTL) is by fabricating hybrid/bi-layer CTLs [21–27]. These CTLs can enhance the optical and electronic properties of the PSC devices leading to enhanced in device performance [25]. "In recent years, multiple studies have shown the advantages of porous NiO$_x$ films as HTL in inverted perovskite solar cells (PSCs). For instance, in 2017, a Que's group employed Ni(OH)$_2$ nanosheets to generate mesoporous structured NiO$_x$ films via high-temperature annealing (500 ºC) of the film and reached a peak power conversion efficiency (PCE) of 11.97 % for a MAPbI$_3$ based PSC [28]. Further, Hong's group, reported the application of p-type nanoporous nickel oxide films as a HTL for fabricating the inverted PSCs and achieved PCE of 19.10 % for (FAPbI$_3$)$_{0.85}$(MAPbBr$_3$)$_{0.15}$ based perovskite absorber [29]. Later, Alex K-Y-Jen's group developed a bilayer structure of NiO$_x$ nanoparticle-based mesoporous and NiO$_x$ blocking layers to enable efficient charge collection at the NiO$_x$/perovskite interface, with a outstanding PCE of 19.6 % for a MAPbI$_3$ based PSC [30]. However, most of these techniques for the fabrication porous NiO$_x$ involved high-temperature annealing or additional additives. In 2019, a low-temperature spray combustion method was reported to fabricate NiO$_x$ thin films, but the device performance remained relatively low (~11.4 %) [31]. Recently, a compact-porous NiO$_x$ HTL was synthesized by using Pluronic P123 as the structure-directing agent and acetylacetone (AcAc) as the coordination agent [32]. This method achieved PCEs of 19.0 % and 21.4 % for PSCs with MAPbI$_3$ and Cs$_{0.05}$(MA$_{0.15}$FA$_{0.85}$)$_{0.95}$Pb(I$_{0.85}$Br$_{0.15}$)$_3$ perovskite compositions, respectively. However, reports on the suitability of porous NiO$_x$ films for wide bandgap applications are still limited."

Here, we report an energy level engineered compact-porous NiO$_x$ (cp-NiO$_x$) layer fabricated by two step spin- and spray-coating techniques with an enhanced electron blocking effect and high transmittance for highly efficient ST-PSCs and TSCs. The compact-NiO$_x$ (c-NiO$_x$) HTL can enable efficient and selective collection of charges from the perovskite layer. The spray-deposition of high crystalline NiO$_x$ colloidal particles led to a mesoporous film which can be used to control the crystallization of the perovskite material and increase the contact area between HTL/perovskite interface. In general, the cp-NiO$_x$ film exhibited superior morphology, better energy level alignment with the perovskite, enhanced average transmittance, and suppressed recombination at the HTL/perovskite interface in comparison with the conventional c-NiO$_x$ HTL. An optimized cp-NiO$_x$ film thickness of ~35 nm enhanced the V_{OC}, suppressed the hysteresis, and reduced optical losses in the NIR region in ST-PSCs leading to an outstanding NIR transmittance of ~92 %, which is desirable for perovskite/silicon TSCs. The performance of the cp-NiO$_x$ HTL based ST-PSC and a 4T perovskite/silicon TSC yielded PCEs of ~15.9 % and ~26.0 %.

2. Experimental section

2.1. Materials

Formamidinium iodide (FAI, > 98 %), methylammonium bromide (MABr, > 98 %) and methylammonium chloride (MACl, > 99 %) were purchased from Greatcell Solar Ltd., Australia. Lead iodide (PbI$_2$, 99.99 %), lead bromide (PbBr$_2$, 99.99 %), and PC$_{60}$BM were purchased from Tokyo Chemical Industry Ltd., Japan. Nickel (II) acetate tetrahydrate ((NiOCOCH$_3$)$_2$.4 H$_2$O), 98 %), cesium iodide (CsI, 99.99 %), dimethylformamide (DMF, anhydrous 99.8 %), dimethyl sulfoxide (DMSO, anhydrous 99.8 %), 2-propanol (IPA, anhydrous 99.5 %) chlorobenzene (CB, anhydrous 99.8 %) were purchased from Sigma Aldrich. Nickel oxide colloidal particles (NiO, 2.5 wt% in ethanol) and zinc oxide (ZnO, 2.5 wt% in 2-propanol) colloidal particles were purchased from Nano Clean Tech. An ITO sputter target (In$_2$O$_3$:SnO$_2$ =90:10 wt%, 99.99 %) was purchased from Dasom rms, Korea.

2.2. Compact-porous NiO$_x$ hole transport layer

Patterned ITO substrates (25 mm × 25 mm) were successively sonicated for 10 min in acetone and ethanol, followed by boiling in 2-propanol for 5 min. After drying, the substrates were UV-Ozone treated for 15 min. The NiO$_x$ sol-gel precursor was prepared by dissolving 24 mg of (NiOCOCH$_3$)$_2$.4 H$_2$O) in 1 mL of ethanol and 5 μL of ethanolamine mixed solvent. The NiO$_x$ precursor was spin-coated onto ITO substrates at 5000 rpm for 30 s, followed by annealing in air for at 350 °C for 30 min in ambient air. Subsequently, a NiO$_x$ colloidal suspension was prepared by diluting 1.0 mL of the as-bought NiO$_x$ colloidal particles (0.3 mg of NiO$_x$) in a mixture of 5 mL of DI water and 5 mL of ethanol (EtOH). The NiO$_x$ colloidal suspension was loaded into the nozzle at a rate of 3.0 mL min^{-1} and was atomized using compressed N$_2$ gas (1.5 kg cm^{-2}). The spray nozzle was scanned at a speed of 1800 mm min^{-1} in a pre-programmed zigzag pattern in x- and y-directions with 2.0 cm spacing at a height of 20.0 cm above the substrates in ambient air without using a hot plate [36]. The samples were annealed on a hot plate at 350 °C for 30 min in ambient air.

2.3. PSC and ST-PSC device fabrication

Opaque perovskite solar cells (PSCs) with a device architecture of glass/ITO/NiOx/perovskite/PC$_{60}$BM/ZnO/Ag were fabricated. For ST-PSCs, the devices were fabricated by replacing the top Ag electrode with a-ITO TCE. The perovskite precursor solution with a composition of Cs$_{0.25}$FA$_{0.75}$PbI$_{2.4}$Br$_{0.6}$ was prepared by dissolving 387.24 mg of PbI$_2$, 132.12 mg of PbBr$_2$, 154.77 mg of FAI, and 77.94 mg of CsI in 1 mL of DMF: DMSO (4:1 v/v) mixed solvent. The perovskite precursor was spin-coated onto the HTL-coated substrates in a two-step process, 1000 rpm for 8 s followed by 5000 rpm for 45 s inside an N$_2$-filled glove box. During the 15 s interval in the second step, 300 μL of CB was dropped onto the substrate. The samples were then annealed at 100 °C for 30 min. The PC$_{60}$BM solution (20 mg/mL in CB) was first spin-coated onto the perovskite layer at 5000 rpm for 40 s. Then, 100 μL of ZnO NPs solution was spin-cast at 2500 rpm for 40 s, followed by annealing at 100 °C for 5 min. For opaque PSCs, 100 nm Ag was deposited onto the device as top contact via thermal evaporation under high vacuum (~2.0 × 10^{-6} torr) condition. For ST-PSC devices, an amorphous indium tin oxide (a-ITO) top transparent conducting electrode (TCE) was used to replace Ag electrode as top contact. The a-ITO TCE was fabricated by first depositing an ~80 nm thick a-ITO film onto the devices using an ultra-high vacuum (~1.0 × 10^{-7} torr) sputtering system (A-Tech System). The sputtering process was conducted at 100 W under Ar:O$_2$ (40:0.2 sccm) flow rate at a working pressure of 1.0 × 10^{-3} Pa.

2.4. Characterization

The structural phase and crystallographic changes of the perovskite films were characterized via XRD (Bruker D8 Advance) using CuKα excitation. The surface morphology and topography of the perovskite films were characterized by FE-SEM (Hitachi SU-70) and AFM (Park Systems NX10). The TEM measurement of NiO colloidal particles was performed using a dark-field- scanning transmission electron microscope (JEM-2010, JEOL). All the previously mentioned research facilities are at the Center for University-wide Research Facilities (CURF) at Jeonbuk National University. A UV–vis spectrometer (PerkinElmer Lambda 750) and a PL spectrometer (Horiba FluroMAx-4) were used for optical absorption and steady-state PL measurements, respectively. XPS and UPS measurements were performed using a Nexsa XPS system (ThermoFisher Scientific UK) system equipped with monochromatized Al K-alpha radiation at hυ = 1486.6 eV for XPS and 21.22 eV for UPS with a base pressure of $\sim 2 \times 10^{-7}$ Torr. The optical absorption and transmittance of the perovskite samples were measured using a UV–vis spectrophotometer (PerkinElmer Lambda 750). J-V curves of the PSCs were measured using a Keithley 2400 source meter SMU instrument (Tektronix Inc.) under simulated one-sun (100 mW/cm^2) illumination from an Oriel Sol AAA solar simulator (Newport Inc.) equipped with a spectral correction filter (AM 1.5G standard). Before conducting the measurements, the intensity of the illumination was calibrated at using a certified NREL silicon cell. EQE spectra of the devices were recorded using an Oriel quantum efficiency measurement device (IQE-200) system under ambient conditions. For SCLC measurements, the dark J–V characteristics of the hole-only devices were measured using a similar Keithley 2400 source meter under dark conditions. Transient photovoltage measurements were conducted using a homemade setup composed of an oscilloscope (Siglent, SDS 1302CFL, 300 MHz with 1 MΩ input) and a function generator (Tektronix, AFG 3022C). A blue laser source of 473 nm (CNI laser, MBL-FN-473) was used as a perturbation source, along with a white LED for background illumination. A time-resolved PL (TRPL) study was performed using an inverted-type scanning confocal microscope (MicroTime-200, Picoquant, Germany) with a 4 × (air) objective. The lifetime measurements were performed using a single-mode pulsed diode laser (470 nm with a pulse width of ~30 ps and an average power of ~100 nW in 200 kHz repetition rate) as an excitation source. A dichroic mirror (490 DCXR, AHF), a long pass filter (FEL0600, Thorlabs), and a single photon avalanche diode (PDM series, MPD) were used to collect emission from the samples. A time-resolved single-photon counting system (TimeHarp-260, PicoQuant GmbH, Germany) was used to count emission photons in a 5 μs time window with a time resolution of 1 ns. Exponential fitting for the obtained phosphorescence decay was performed using Symphotime-64 software (Ver. 2.2).

The sizes of the cells crystalline SiSC was 2 cm × 2 cm from a 6 in.-diameter wafer. The performance of filtered bottom SiSC in a 4 T tandem cell was measured using the c-NiO$_x$ and cp-NiO$_x$ HTL-based ST-PSC as an optical filter. The J–V and EQE measurement of SiSC and ST-PSC were conducted separately, and the SiSC was characterized by mechanically stacking a perovskite optical filter on top maintaining a 0.5 mm air gap between the ST-PSC filter and the SiSC.

3. Results and discussion

For the fabrication of ST-PSCs, we designed a cp-NiO$_x$ HTL scheme that consists of compact and mesoporous NiO$_x$ films. The HTLs were sequentially fabricated by sol-gel and spray deposition techniques using NiO precursor salt and crystalline NiO$_x$ colloidal particles, respectively, as displayed in Fig. 1a. A device architecture of ITO/cp-NiO$_x$/perovskite/PC$_{60}$BM/ZnO NPs/a-ITO was fabricated for ST-PSC demonstration (Fig. 1a). A photo-stable cesium (Cs) and bromide (Br) rich perovskite composition of Cs$_{0.25}$FA$_{0.75}$PbI$_{0.8}$Br$_{0.2}$ used in this work has an optical E_g of ~1.68 eV [33]. The NiO$_x$ colloidal particle spray-coating parameters were first optimized in terms of device performance. The optimum device performance was obtained for ~6 spray cycles (Fig. S1). Details of the fabrication process can be found in the experimental section.

For physical characterization of the cell structure, field-emission scanning electron microscopy (FE-SEM) cross-sectional imaging was used as displayed in Fig. 1b. The cp-NiO$_x$ HTL between the indium tin oxide (ITO) and perovskite layers can be easily observed. The dense and uniform perovskite layer (~500 nm) deposited on the cp-NiO$_x$ HTL was confirmed. Fig. 1c shows photocurrent density-voltage (J-V) curves for the c-NiO$_x$ and cp-NiO$_x$ HTL based ST-PSCs. The cp-NiO$_x$ HTL based ST-PSC shows an V_{OC} of 1.10 V, a short-circuit (J_{SC}) of 18.56 mA/cm2, and a fill factor of 78.1 %, giving an overall PCE of 15.95 % (Table 1), whereas the c-NiO$_x$ HTL based ST-PSC shows an overall PCE of 13.9 %, with a V_{OC} of 1.04 V, a J_{SC} of 18.2 mA/cm^2, and a fill factor of 73.3 %. It is to be note that ST-PSC device based on p-NiOx showed similar performance of ~14 % (Fig. S2). Additionally, the average PCE for 35 cells based on cp-NiO$_x$ HTL was 15.1%, which was higher than that of cells based on c-NiO$_x$ HTL (avg. PCE ~ 13.2 %) as displayed in the histogram (inset of Fig. 1c). We observed that a higher V_{OC} of 1.1 V was obtained using the cp-NiO$_x$ HTL, which led to the overall higher performance of the ST-PSC. A cp-NiO$_x$ HTL over an opaque PSC device was also investigated. The best PSC based on the cp-NiO$_x$ HTL yielded a PCE of ~17.8 %, which was ~10 % higher than the c-NiO$_x$ HTL based PSC (PCE ~16.1 %) (Fig. S3). Moreover, the cp-NiO$_x$ HTL based PSC devices also demonstrated lower hysteresis in PSCs. The device parameters obtained in both in reverse- and forward-scan directions are summarized in Table S1. The cp-NiO$_x$ HTL based device exhibited PCEs of ~17.8 % and ~16.8 % in reverse- and forward-scan directions, respectively, with a negligible hysteresis index (HI) of 0.059 compared to the c-NiO$_x$ HTL based device (HI ~0.093) (Fig. S3) as extracted from the PCE measured under the forward and reverse scan (Expression S1). This confirms that there is a reduced capacitive effect shown by the PSCs based on cp-NiO$_x$ HTL. High annealing temperatures (~350 °C) can lead to sintering at the interface between the compact and mesoporous films and improve the charge transfer property at the interface of the sol-gel and colloidal suspension-based NiO$_x$ HTLs. The external quantum efficiency (EQE) spectra of the PSCs based on the NiO$_x$ HTL is displayed in Fig. S4. The integrated photocurrent density calculated using the EQE spectrum matched well with the J_{SC} values obtained from the J-V measurements. The EQE spectra of the cp-NiO$_x$ HTL based PSCs showed a superior photon-to-current conversion efficiency compared with the c-NiO$_x$ HTL based PSCs. The integrated J_{SC} value determined by the EQE data were 18.7 and 19.2 mA /cm^2 for c-NiO$_x$ and cp-NiO$_x$ based devices, respectively. Therefore, the EQE enhancement could be attributed to improved charge collection, confirming that the cp-NiO$_x$ HTL can lead to enhanced device performance.

To understand the better performance of the cp-NiOx HTL based ST-PSCs, we explored the optical and structural properties of the HTLs. Fig. 2a shows total transmittance spectra of the c-NiO$_x$ and cp-NiO$_x$ HTL deposited over ITO substrates. The c-NiO$_x$ and cp-NiO$_x$ films showed transmittances of ~82 % and ~83 % at 550 nm, respectively. Interestingly, the c-NiO$_x$ and cp-NiO$_x$ films also showed average transmittances (AVTs) of ~82 % and ~83 % from 750 nm to 1200 nm, respectively. Most importantly, the overall transmittance of the cp-NiO$_x$ was uncompromised by the increase in thickness after additional deposition of the NiO$_x$ colloidal particles. Rather, the cp-NiO$_x$ exhibited a significant enhancement (~2.3 %) in its transmittance spectrum in the visible region (380–750 nm) [34]. This is possibly because an increase in the NiO$_x$ film thickness enables stronger light propagation and photon oscillation [31]. Basically, the thickness of the cp-NiO$_x$ HTL increased consecutively with an
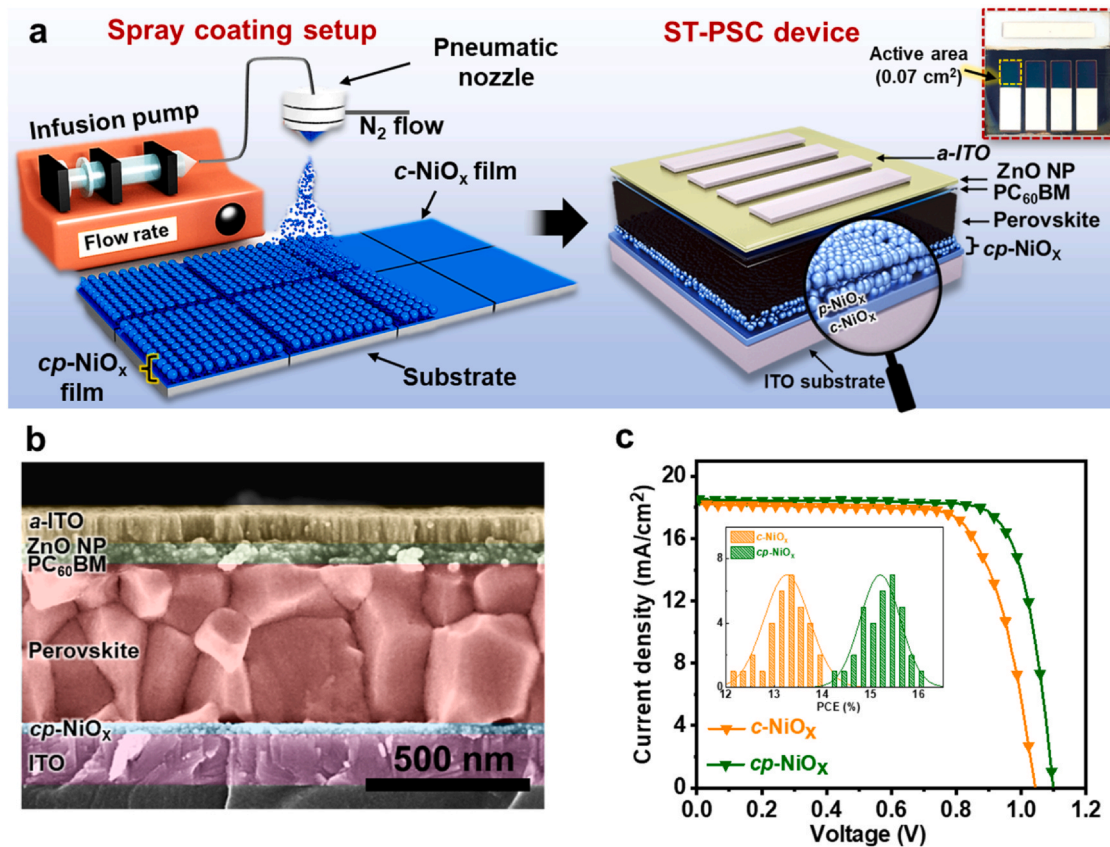
Fig. 1. (a) Schematic illustration for fabrication of ST-PSC based on cp-NiO$_x$ HTL, (b) cross-sectional FE-SEM images of the cp-NiO$_x$ HTL based ST-PSC device. (c) Current density and voltage curves of ST-PSCs based on the c-NiO$_x$ and cp-NiO$_x$ HTLs (inset shows average PCE distribution).

Table 1

Device performance of SiSC,STPSC, and perovskite/silicon devices based on the c-NiO$_x$ and cp-NiO$_x$ as HTLs.

Device	V_{OC} [V]	J_{SC} [mA/cm^2]	FF [%]	PCE [%]
ST-PSC	1.044	18.20	73.31	13.93
Filtered SiSC	0.680	19.78	71.38	9.60
4 T TSC	-	-	-	23.53
ST-PSC	1.10	18.56	78.13	15.95
Filtered SiSC	0.689	20.64	70.74	10.06
4 T TSC	-	-	-	26.01

increase in the number of spray cycles. Correspondingly, the total transmittance of the cp-NiO$_x$ HTL changed with the increase in the total thickness. The change in total transmittance of the cp-NiO$_x$ layer was investigated by analyzing the transmittance spectra of cp-NiO$_x$ films spin-coated over the ITO substrate (Fig. S5). As a proof of concept, finite-difference time-domain simulations were conducted to successfully confirm our experimental observation of the optical transmittance spectra of the c-NiO$_x$ and cp-NiO$_x$ films on the ITO substrate (Fig. S6). The Tauc plots for the c-NiO$_x$ and cp-NiO$_x$ films are plotted using the transmittance spectrum (inset of Fig. 2a). The optical bandgap of the c-NiO$_x$ and cp-NiO$_x$ films were found to be ~4.16 eV and ~4.0 eV, respectively. Further, the X-ray diffraction (XRD) measurement revealed that the pristine NiO$_x$ colloidal particles films exhibited broad and subtle diffraction peaks at $2\theta \sim 37.3°$ and $\sim 43.7°$, which correspond to the (111) and (200) planes of a cubic crystal structure (JCPDS card No. 47–1049) indicating the crystalline nature (Fig. S7) [35]. The crystallinity of the c-NiO$_x$ and cp-NiO$_x$ films was analyzed by XRD patterns as shown in Fig. 2b. The XRD spectrum of c-NiO$_x$ film showed a peak at $2\theta \sim 43°$, whereas, the cp-NiO$_x$ film showed relatively stronger peaks at $2\theta \sim 37.3°$ and $\sim$

43.7°, which correspond to the (111) and (200) planes. Highly crystalline cp-NiO$_x$ HTL is favorable for PSC applications because it exhibits fewer defects than the sol-gel processed c-NiO$_x$ HTL. Consequently, the crystallinity and particle size of NiO$_x$ colloidal particles were examined using high-resolution-transmission electron microscopy (HR-TEM) measurements. The HR-TEM images of the colloidal particles are displayed in Figs. 2c and 2d. The colloidal suspension consisted of colloidal particles having average sizes of ~7–10 nm. Additionally, the histogram plot for the distribution of the colloidal particle size is presented in Fig. S8. Lattice fringes with interplanar spacings of 2.5 Å, 2.1 Å, and 1.73 Å corresponding to (111), (200), and (220) crystal planes, respectively, were observed. Selected-area electron diffraction (SAED) patterns also revealed a set of distinct rings composed of diffraction spots (inset of Fig. 2d), which can be assigned to the (111), (200), and (220) planes. The XRD patterns and HR-TEM measurements confirmed the extremely high crystallinity of the NiO$_x$ colloidal particles, which are necessary for fabricating highly efficient PSCs. Moreover, the small size of NiO$_x$ colloidal particles used here resulted in good dispersibility of the colloidal suspension for spray-coating applications used to fabricate uniform NiO$_x$ films without any aggregates [36]. XPS characterization was conducted to further understand the elemental composition of the non-stoichiometric NiO$_x$ films. The survey scans of both c-NiO$_x$ and cp-NiO$_x$ shows that all the peaks of Ni and O are presented in Fig. S9. The Ni2p spectra and O1s characteristic peaks and their corresponding deconvoluted curves are displayed in Figs. 2e and 2 f, respectively, and the deconvoluted parameters are summarized in Table S2. Core level spectra of Ni $2p_{1/2}$ and $2p_{3/2}$ showed the doublet states of nickel, Ni^{2+} and Ni^{3+} from lower to higher binding energy, respectively. In the Ni2p spectra of the cp-NiO$_x$, the binding energies of the Ni^{2+} and Ni^{3+} of NiO and Ni$_2$O$_3$ were around 854.2 eV and 856.0 eV, respectively [37,38]. The total integral area ratio of Ni^{3+} and
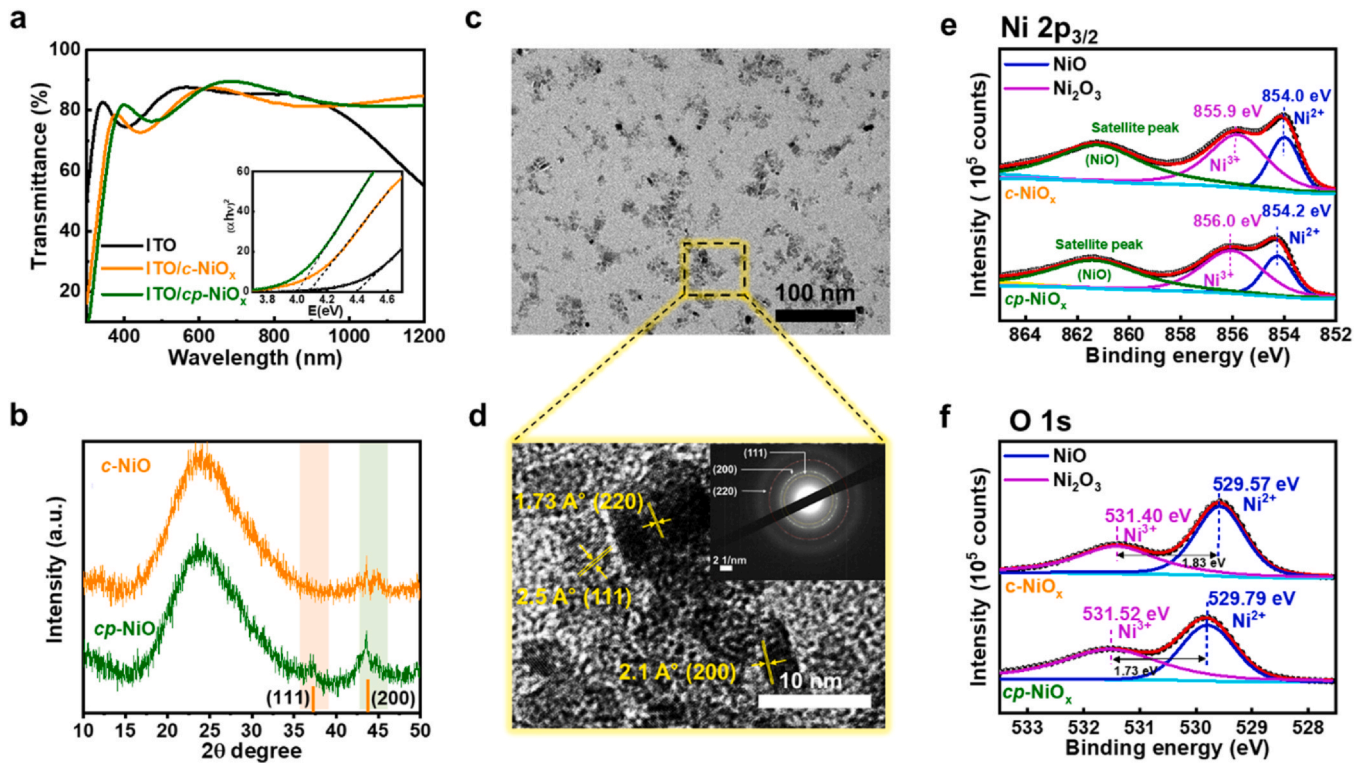
Fig. 2. (a) Transmittance spectra, and (b) XRD patterns of the c-NiO$_x$ and cp-NiO$_x$ films coated over the ITO substrate. (c) and (d) show low magnification TEM images and corresponding HR-TEM images of NiO colloidal particles with scale bars of 100 nm and 10 nm, respectively (inset shows SAED pattern of NiO colloidal particles in the colloidal suspension). (e) Ni 2p XPS spectrum and (f) O1s XPS spectrum of the c-NiO$_x$ and cp-NiO$_x$ films.

Ni^{2+} (Ni^{3+}/Ni^{2+}) were determined to be 1.38 and 1.32 for c-NiO$_x$ and cp-NiO$_x$ films, respectively. The presence of the Ni^{3+} state in Ni$_2$O$_3$ is a result of the oxygen deficiency in NiO, indicating the presence of a Ni vacancy. The slightly higher Ni^{3+} ratio in the c-NiO$_x$ sample may contribute to the increase in the hole conductivity due to the increased concentration of oxygen vacancies, which act as hole carriers. Therefore, the c-NiO$_x$ film improves its hole conductivity by increasing the concentration of Ni vacancies, which lead to an increase in the Ni^{3+}/Ni^{2+} ratio [39]. Therefore, we concluded that the p-type conductivity was higher for the c-NiO$_x$ film compared to the cp-NiO$_x$ film. However, it has also been demonstrated that Ni^{3+} surface species can result in the formation of the A-site cation-deficient perovskite at the NiO$_x$/perovskite interface. This defective PbI$_{2-x}$Br$_x$-rich perovskite forms an energetic barrier limiting the efficient hole extraction process and increasing the recombination at the NiO$_x$/perovskite interface, resulting in V_{OC} losses in PSCs [40]. The higher value of Ni^{3+}/Ni^{2+} for the c-NiO$_x$ films suggests the possibility of higher defects buried under the c-NiO$_x$/perovskite interface, which can lead to the lower V_{OC} of the perovskite devices.

Next, we conducted a systematic study of the morphology and topological properties of the c-NiO$_x$ and cp-NiO$_x$ films. The surface morphologies of the c-NiO$_x$ and cp-NiO$_x$ HTLs over the ITO substrates are displayed in Figs. 3a and 3b. The c-NiO$_x$ film exhibited a compact morphology of small particulates with a film thickness of ~20 nm (Fig. S10). A total optimized thickness of ~35 nm was obtained after spray-coating of the NiO$_x$ colloidal suspension over the ~20 nm thick c-NiO$_x$ film. The morphology of the cp-NiO$_x$ film had a relatively loose texture and mesoporous morphology in comparison to its highly compact counterpart. A spray-coating technique was employed in this work due to its ability to fabricate highly uniform NiO$_x$ nanostructured films with pinhole-free, meso-porous like morphologies compared to spin-coated technique-based NiO$_x$ films. Granular-like structures were not observed in the spin-coated NiO$_x$ colloidal particle-based films, confirming that the granular

structures were only formed via spray-deposition as displayed in Fig. S11 [41]. Next, the atomic force microscope (AFM) topographical images of both the c-NiO$_x$ and cp-NiO$_x$ films were analyzed as displayed in Fig. 3c and d, respectively. The cp-NiO$_x$ film root mean square (RMS.) roughness was ~9.1 nm, which is higher than the of c-NiO$_x$ film (RMS roughness ~6.4 nm). The granular morphology of the cp-NiO$_x$ film can be regarded as a mesoporous morphology that can improve the contact area between NiO$_x$ HTL and perovskite directly favoring interfacial charge transfer. Usually, porous films have a rougher morphology which could easily induce pinholes in the perovskite film. Therefore, to analyze the effect of the two HTLs on the formation of the perovskite film, we analyzed FE-SEM images of the perovskite films on the c-NiO$_x$ and cp-NiO$_x$ films. Highly crystalline and uniform perovskite films were fabricated using the one-step/anti-solvent dripping technique. Fascinatingly, nucleation growth and morphological characteristics of perovskite films were found to be highly susceptible to the surface properties of the bottom substrate as displayed in the FE-SEM images of perovskite films fabricated over c-NiO$_x$ and cp-NiO$_x$ films in Fig. 3e and f, respectively. [32]. The perovskite layer coated over the cp-NiO$_x$ layer displayed an average grain size of ~280 nm, which is relatively more uniform and larger than the perovskite coated over the c-NiO$_x$ layer, which had an average grain size of ~190 nm. The respective average grain size histogram plots for the perovskite layers deposited on each HTL are displayed in Fig. S12. This behavior is probably due to the adequate compromise between hydrophobicity and hydrophilicity in the cp-NiO$_x$ layer, which satisfies heterogeneous nucleation and was confirmed through the contact angle analysis as displayed in inset of Fig. 3a and b [32]. No additional treatments were used in this work to make the NiO$_x$ surface hydrophilic before coating the perovskite precursor over the NiO$_x$ layer which makes the nucleation of the perovskite grains more susceptible to the surface energy of the NiO$_x$ films. Water contact angle measurements were conducted for the NiO$_x$ films. The c-NiO$_x$ film had a water
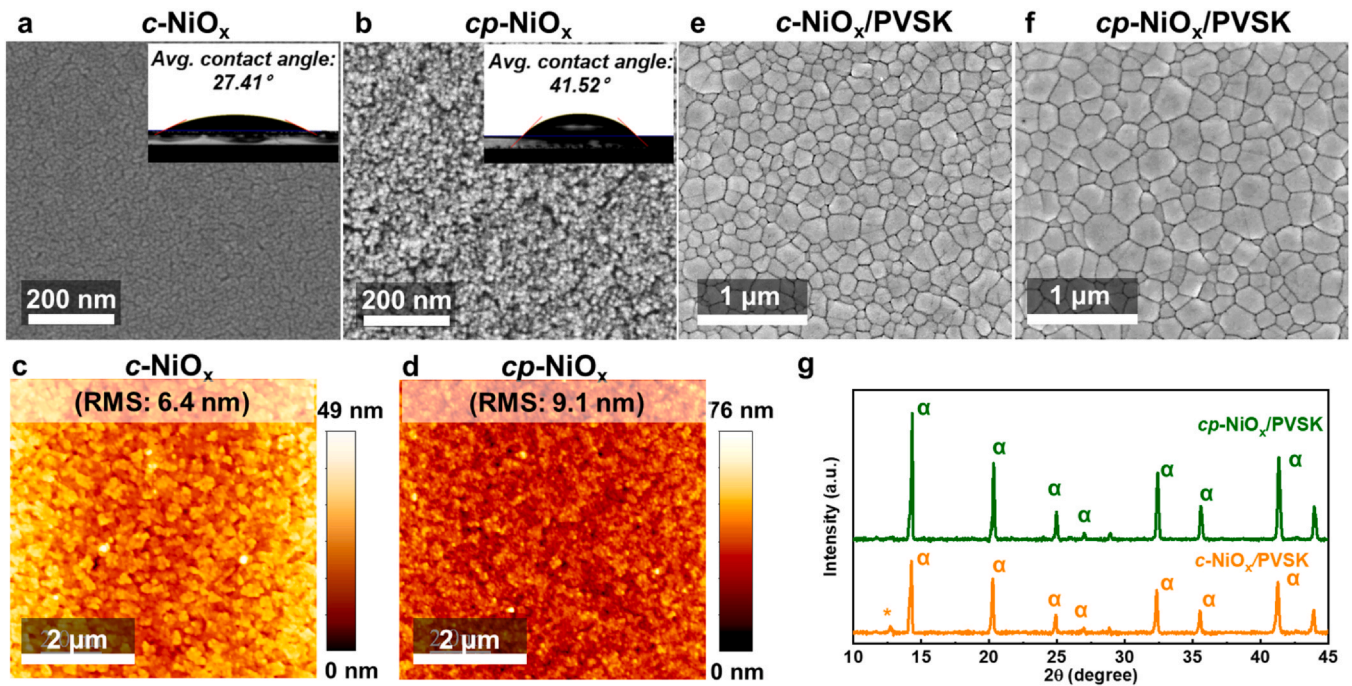
Fig. 3. (a), (b) FE-SEM images, (c), and (d) AFM topographic images of the c-NiO$_x$ and cp-NiO$_x$ films, respectively. FE-SEM images of the perovskite films (e) c-NiO$_x$ and (f) cp-NiO$_x$ films. (g) XRD pattern of the perovskite films deposited over the c-NiO$_x$, and cp-NiO$_x$ films.

contact angle (WCA) of 27.41°. After spray-coating the NiO$_x$ colloidal suspension, the surface became more hydrophobic as confirmed by the WCA of 41.52° of the cp-NiO$_x$ film. Further, the crystallinity of the perovskite films fabricated over the two NiO$_x$ films were investigated and are displayed in Fig. 3g. The 2θ position of 14.2° represents the formation of the α (110) black perovskite phase. Fascinatingly, the ratio of the intensity of the peaks at the 2θ position of 14.2° for the cp-NiO$_x$ and c-NiO$_x$ was calculated to be ~1.62, confirming the higher crystallinity of the perovskite film fabricated over the c-NiO$_x$. Additionally, a small peak at the 2θ position of 12.6° was observed for the perovskite film coated over the c-NiO$_x$. This peak at the 2θ position of 12.6° signifies the excess PbI$_2$ content in the bulk perovskite film. This remnant PbI$_2$ in the bulk perovskite film is highly undesirable as the high bandgap of PbI$_2$ (~2.3 eV) possibly induces potential barriers at the extraction layers, induces carrier accumulation at the interface, hinders the charge transport, and is responsible for accelerated degradation of the perovskite layer on exposure to moisture and light [42]. However, this remnant PbI$_2$ almost disappeared in the XRD pattern of the perovskite film fabricated over the cp-NiO$_x$ film pointing towards the better hole extraction possibility at the cp-NiO$_x$/perovskite interface.

A general hint of superior hole extraction at the cp-NiO$_x$/perovskite interface was provided by the XRD pattern of the perovskite film fabricated over the cp-NiO$_x$ film. However, the exacted interfacial properties at the buried interface between the HTLs and perovskite remain ambiguous. Thus, we further investigated the absorbance spectra of the perovskite films fabricated over the c-NiO$_x$ and cp-NiO$_x$ films (Fig. S13). As observed from the absorbance spectrum of the perovskite layers coated over the two NiO$_x$ films, there was no change in the optical bandgap of the perovskite film. Interestingly, the optical absorption of the perovskite films coated over the NiO$_x$ film increased marginally which could be due to the slightly enhanced photon flux received by the perovskite layer as already confirmed from the transmittance spectra of the NiO$_x$ films (Fig. 2a). Further, ITO/NiO$_x$/perovskite samples were prepared to study the behaviors of the charge carriers on short-time scales. The PL emission of the film was quenched significantly because of charge transfer at the NiO$_x$/perovskite interface. Fig. 4a clearly

indicates the superior hole extraction capacity of both the c-NiO$_x$ and cp-NiO$_x$ films. Moreover, transient photoluminescent (TRPL) measurements were performed to probe the charge transfer dynamics at the NiO$_x$/perovskite interface. The TRPL transients for perovskite layers coated over the c-NiO$_x$ and cp-NiO$_x$ films are displayed in Fig. 4b. The PL measured on the perovskite film coated over the NiO$_x$ films decayed bi-exponentially and was calculated using exponential fitting (Expression S2). The average fluorescence decay lifetime (τPL) of the c-NiO$_x$/perovskite and cp-NiO$_x$/perovskite samples reduced from 27.2 ns to 24.0 ns, respectively (Table S3), indicating that there exists better charge transfer across the cp-NiO$_x$/perovskite interface. The slightly shorter τPL of the cp-NiO$_x$/perovskite interface compared to the c-NiO$_x$/perovskite counterpart showed reduced charge trapping defects at the HTL/perovskite interface. Generally, NiO$_x$ prevents the direct contact of the perovskite layer with ITO and improves the alignment of valence band maximum (VBM) to enlarge the quasi-Fermi-level splitting (QFLS) which led to higher V_{OC} [43]. To assess the energetic properties of the c-NiO$_x$ and cp-NiO$_x$ films with the perovskite absorber, we performed ultra-violet photoelectron spectroscopy (UPS) on c-NiO$_x$, cp-NiO$_x$, and perovskite samples. The UPS spectra for the c-NiO$_x$ and cp-NiO$_x$ films are displayed in Fig. 4c. Additionally, the UPS spectra for the wide-bandgap perovskite film are displayed in Fig. S14. All the calculated parameters of the E$_{VBM}$, and E$_{CB}$ for all the samples are summarized in Table S4. Based on Expression S3, the valence band energy levels (E$_{VBM}$) of the c-NiO$_x$ and cp-NiO$_x$ films were calculated to be 5.35 eV and 5.58 eV, respectively [44]. Based on the values of E_g derived from the Tauc plot and the E$_{VBM}$ values obtained from the UPS spectra, a summary of the results is schematically displayed as the energy band diagrams of the samples in Fig. 4d with reference to the vacuum level. On comparing the valence band onset of the perovskite absorber to the E$_{VBM}$ levels of the HTLs, the c-NiO$_x$ was found to possess a higher energetic barrier for electrons (~1.27 eV) among the two HTLs. On the other hand, cp-NiO$_x$ showed the closest alignment to the E$_{VBM}$ of the perovskite. The closeness of the E$_{VBM}$ of the HTL to the perovskite's E$_{VBM}$ could facilitate the extraction of holes from the perovskite. Based on this energetic scheme, the c-NiO$_x$ showed larger offset in E$_{VBM}$, and the cp-NiO$_x$ films showed
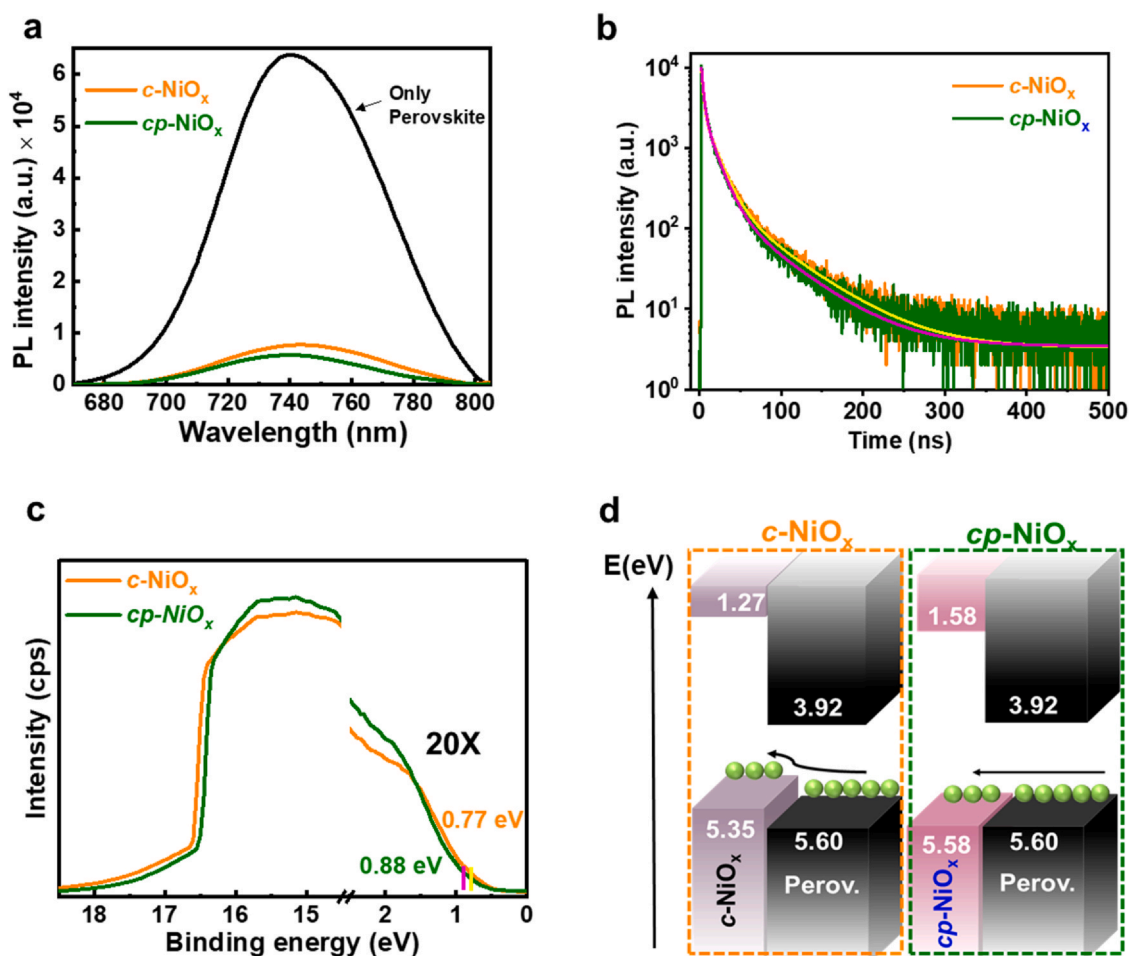
Fig. 4. (a) Steady-state PL spectra, and (b) logarithmic plot of the normalized TRPL spectra of the perovskite films coated over the c-NiO$_x$ and cp-NiO$_x$ films, respectively. (c) UPS spectrum depicting the cut-off energy and off-set energy of the c-NiO$_x$, and cp-NiO$_x$ films. (d) A schematic illustration of the possible band alignment of NiO$_x$ and perovskite layer according to their valence bands.

negligible offset to the perovskite E_{VBM}, which may result in higher V_{OC} when cp-NiO$_x$ is used as HTL for fabricating PSCs.

Transient photovoltage (TPV) measurements were conducted to better understand the quality of perovskite films (i.e., the charge trap-state densities) deposited on the cp-NiO$_x$ HTL, by studying the carrier recombination kinetics and carrier recombination lifetimes (τ_{rec}) of both the NiO$_x$ HTLs-based devices. The decay profiles of these devices are displayed in Fig. S15. The cp-NiO$_x$ HTL-based ST-PSCs exhibited longer decay profile (τ_{rec} of ~2.39 µs measured at 1/e) compared to the c-NiO$_x$, which had a comparatively shorter decay profile τ_{rec} of ~1.38 µs (Table S5). This indicates that the cp-NiO$_x$ based PSC exhibits longer carrier lifetime, which might have resulted from the reduced trap density in the perovskite layer and the HTL/perovskite interface [45]. Further, the charge dynamics of the PSCs based on NiO$_x$ HTLs is studied from the dark J-V characteristics hole-only devices by space charge limited current (SCLC) measurements. For this, hole-only devices having a device structure of ITO/NiO$_x$/perovskite/PTAA/a-ITO were fabricated. Typically, three regions are distinctly visible in dark J-V curves in a log-log representation, as shown Fig. S16. The low-bias region represents an ohmic contact with the electrode, while the current density increased abruptly with the increasing bias, corresponding to a trap-filled limit (TFL) current. The trap-filled limited voltage (V_{TFL}) values for c-NiO$_x$ and cp-NiO$_x$ HTL were determined to be 0.72 V and 0.61 V, respectively. The trap density (N_{trap}) was calculated using the Mott-Gurney relation (Expression S4) are to be 5.7×10^{16} cm^{-3} and 4.8×10^{16} cm^{-3} for c-NiO$_x$ and cp-NiO$_x$ HTL based hole only devices, respectively.

The lower trap density in the cp-NiO$_x$ HTL based device can be ascribed to the higher crystallinity of the NiO$_x$ colloidal particles present in contact with the perovskite layer. We further investigate the internal charge transfer dynamics of PSC devices using electrochemical impedance spectroscopy (EIS) measurements performed under dark condition at a constant bias of 0.9 V. The Nyquist plots of the PSCs based on the c-NiO$_x$ and cp-NiO$_x$ HTLs are displayed in Fig. S17. The high frequency arc is associated with the charge transfer resistance (R_{CT}), and the lower frequency arc is assigned to recombination resistance (R_{REC}) at HTL/perovskite interface. The cp-NiO$_x$ based PSC shows the least resistance in charge transfer as confirmed by the radius of semicircle in the high frequency range. Moreover, the radius of semicircles in the low frequency region confirms that cp-NiO$_x$/perovskite interface offers higher charge recombination resistance compared to the c-NiO$_x$/perovskite interface. The values of R_{CT} and R_{REC} for each PSC were extracted by fitting their corresponding Nyquist curves using the circuit model depicted in the inset of Fig. S17. The extracted values of R_{REC} for PSCs based on c-NiOx and cp-NiOx HTLs were ≈ 105 Ω and ≈ 243 Ω, respectively. All these characterizations have simultaneously confirmed that the cp-NiO$_x$ can extract charge better than the c-NiO$_x$ at the HTL/perovskite interface that led to better device performance.

Wide-band-gap PSCs have primary applications as semi-transparent PVs and tandem cells. To further confirm the efficacy of the ST-PSC based on cp-NiO$_x$ HTL a 4 T perovskite/silicon TSC was demonstrated by mechanically stacking the ST-PSC optical filter over a SiSC and measuring the SiSCs performance. The ~500 nm thick
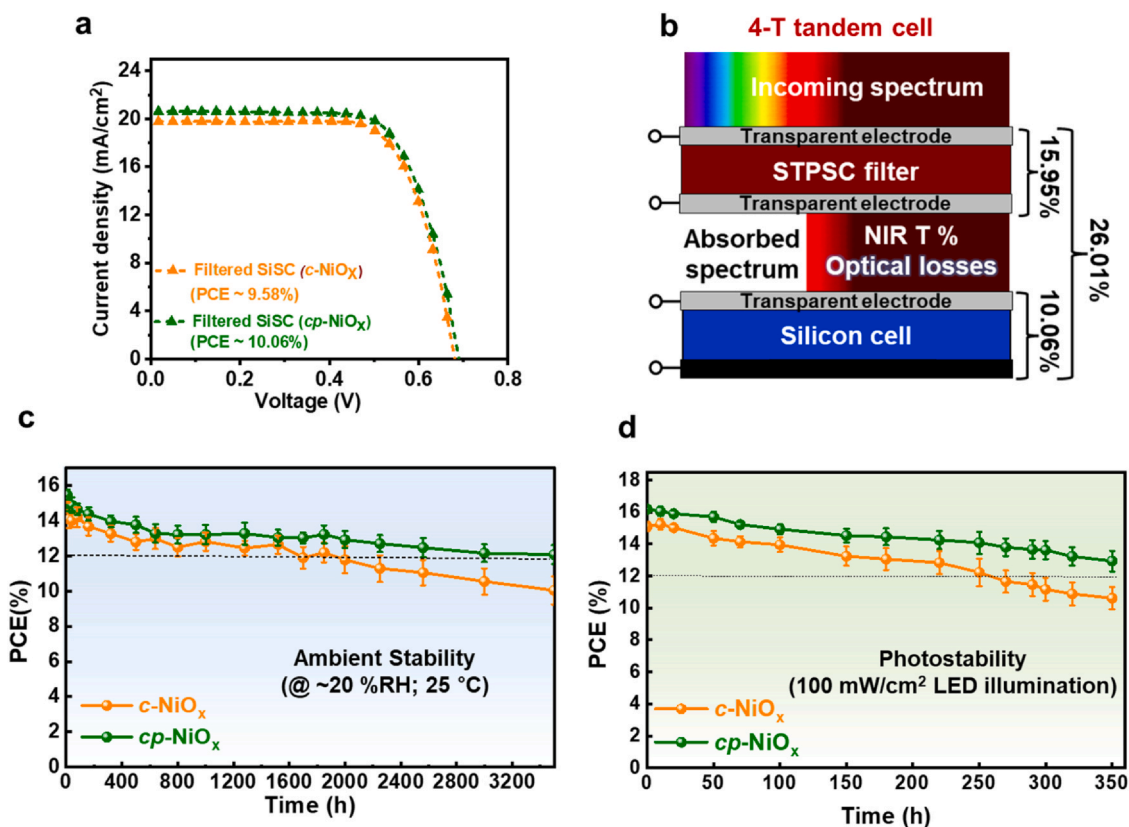
Fig. 5. (a) The current density-voltage characteristics of SiSCs filtered through ST-PSCs fabricated using *c*-NiO$_x$ and *cp*-NiO$_x$ HTLs. (b) A schematic illustration showing the testing scheme for the 4 T ST-PSC/SiSC stacked tandem solar cells. PCE variations of the ST-PSCs based on *c*-NiO$_x$ and *cp*-NiO$_x$ HTLs as a function of storage duration (c) in ambient air and (d) under 100 mW/cm^2 white LED illumination.

perovskite film with a wide-bandgap of ~1.68 eV ensured adequate absorption for λ < 800 nm and adequate transmittance for λ > 800 nm. Nevertheless, the parasitic optical losses in charge transport layers lead to reduced transmittance for λ > 800 nm. The total transmittance of *c*-NiO$_x$ and *cp*-NiO$_x$ HTL based ST-PSCs were measured to explore the effect of the two NiO$_x$ HTLs over the optical transmittance of the ST-PSC device (Fig. S18). Interestingly, the average transmittance values (AVT%) in the wavelength range of 800–1200 nm of the ST-PSCs fabricated using *c*-NiO$_x$ and *cp*-NiO$_x$ were ~86 %, and ~92 %, respectively. On illuminating the rear glass of the ST-PSC most of the high energy photons were absorbed by the perovskite layer, and the photons with lower energies proceed through the front surface towards the SiSC. The *J-V* characteristics of the SiSC (PCE of ~19.90%) used for this work are displayed in Fig. S19. The PCE of the SiSC filtered using the ST-PSCs (optical filters) based on the *c*-NiO$_x$ and *cp*-NiO$_x$ HTL are displayed in Fig. 5a, and their respective photovoltaic parameters are summarized in Table 1. The PCE yield of the SiSC filtered using *cp*-NiO$_x$ HTL based ST-PSC was ~10.0 %, which was higher than the PCE obtained using *c*-NiO$_x$ HTL based ST-PSC optical filters (~9.6 %). A similar trend demonstrating enhanced current density was obtained from the EQE spectra of the filtered SiSC (Fig. S18). Further, we summarized the PCE and NIR transparency ST-PSC devices fabricated in this work with published reports in Table S6. The excellent NIR transparency of the PCE trade-off observed in the *cp*-NiO$_x$ HTL based ST-PSCs led to a PCE of ~26.0 % for the 4T perovskite/silicon TSC yielding, which is a ~10% enhancement compared to the *c*-NiO$_x$ HTL based TSC. Moreover, the performance of *cp*-NiO$_x$ HTL based 4T perovskite/silicon TSC is on par with the reports and can further be improved using more efficient bottom cells.

The stability of the ST-PSCs is also a crucial factor from a commercialization point of view. Therefore, the stability of ST-PSCs based on the *c*-NiO$_x$ and *cp*-NiO$_x$ HTLs was explored. In general, perovskite devices having ITO applied as top the electrode will have better stability and moisture resistance [46]. We simply dropped water over PSC devices with and without an *a*-ITO top electrode. The film without the *a*-ITO electrode immediately degraded as the water molecules easily reach the perovskite layer and irreversibly destroy it. In contrast, the PSC with *a*-ITO top electrode maintains its form (Fig. S20). The ambient stability was tested at room-temperature of ~25 °C and relative humidity (RH) of ~20 % as displayed in Fig. 5c and photostability was measured under the 1 sun illumination. The ambient stability of ST-PSC cells based on the *c*-NiO$_x$ and *cp*-NiO$_x$ showed PCE retentions of ~68 % and ~77 % after 3500 h, respectively. Evidently, ST-PSCs based on *cp*-NiO$_x$ HTL demonstrated improved photostability, showing a PCE retention of > 80 % after 350 h of continuous illumination (100 mW/cm^2) by a white LED. In contrast, ST-PSC based on the *c*-NiO$_x$ demonstrated a PCE retention of only 70.68 % subjected to the same condition (Fig. 5d). The different degradation rates of the ST-PSCs based on *c*-NiO$_x$ and *cp*-NiO$_x$ HTLs can possibly be explained using the XRD spectra (Fig. 2f) of the perovskite films deposited over each HTL. After the ST-PSC devices are constantly illuminated from the bottom ITO side, the minor amount of unreacted PbI$_2$ observed in the XRD spectrum of the perovskite film (Fig. 3g) deposited over the *c*-NiO$_x$ can accelerate the degradation process [42].

4. Conclusion

This work demonstrated the fabrication of a dopant-free, highly transparent compact-porous-NiO$_x$ HTL for applications in ST-PSCs and perovskite/silicon TSCs. The *cp*-NiO$_x$ HTL was sequentially fabricated by sol-gel and spray deposition techniques using NiO$_x$ precursor salt and highly crystalline NiO$_x$ colloidal particles,

respectively. The *cp*-NiO$_x$ film demonstrated a mesoporous and pin-hole-free morphology, enhanced transmittance, better energy band alignment with perovskite layer, and control over the formation of the perovskite films. The device performance of ST-PSCs based on *cp*-NiO$_x$ HTL was investigated taking compact-NiO$_x$ HTL as a reference. The ST-PSCs based on *cp*-NiO$_x$ HTL demonstrated reduced charge recombination at the HTL/perovskite interface and higher NIR transmittance leading to the best PCE of 15.9 % and a PCE of ~26.0 % when mechanically integrated with SiSC to form 4T perovskite/silicon TSCs. The ST-PSCs also demonstrated great PCE retention in ambient conditions and continuous light illumination. This work demonstrated the facile fabrication of highly transparent and efficient *cp*-NiO$_x$ HTLs, which have the potential for fabricating highly efficient, and stable inverted ST-PSCs and perovskite/silicon TSCs.

CRediT authorship contribution statement

B.T.: Conceptualization, methodology, formal analysis, investigation, writing—original draft. **N.K.**: Methodology, Formal analysis. **H.B.L**: Formal analysis. **Y.M.S**: Optical simulation analysis. **S.C.**: TRPL analysis. **J.S.**: TRPL analysis. **J.-W.K**: Conceptualization, supervision, funding acquisition, writing—review and editing.

Data availability

No data was used for the research described in the article.

Declaration of Competing Interest

The authors declare that they have no known competing financial interests or personal relationships that could have appeared to influence the work reported in this paper.

Acknowledgments

Appendix A. Supporting information

Supplementary data associated with this article can be found in the online version at doi:10.1016/j.jallcom.2023.170970.

References

[1] W. Shockley, H.J. Queisser, Detailed balance limit of efficiency of p-n junction solar cells, J. Appl. Phys. 32 (1961) 510–519.

[2] NREL solar cell efficiency chart , 2023.

[3] J.H. Noh, S.H. Im, J.H. Heo, T.N. Mandal, S. Seok II, Seok, chemical management for colorful, efficient, and stable inorganic–organic hybrid nanostructured solar cells, Nano Lett. 13 (2013) 1764–1769.

[4] G.E. Eperon, S.D. Stranks, C. Menelaou, M.B. Johnston, L.M. Herz, H.J. Snaith, Formamidinium lead trihalide: a broadly tunable perovskite for efficient planar heterojunction solar cells, Energy Environ. Sci. 7 (2014) 982.

[5] R.J. Sutton, G.E. Eperon, L. Miranda, E.S. Parrott, B.A. Kamino, J.B. Patel, M.T. Hörantner, M.B. Johnston, A.A. Haghighirad, D.T. Moore, H.J. Snaith, Bandgap-tunable cesium lead halide perovskites with high thermal stability for efficient solar cells, Adv. Energy Mater. 6 (2016) 1502458.

[6] Z. Li, B. Li, X. Wu, S.A. Sheppard, S. Zhang, D. Gao, N.J. Long, Z. Zhu, Organometallic-functionalized interfaces for highly efficient inverted perovskite solar cells, Science 376 (2022) 416–420.

[7] F. Ma, Y. Zhao, J. Li, X. Zhang, H. Gu, J. You, Nickel oxide for inverted structure perovskite solar cells, J. Energy Chem. 52 (2021) 393–411.

[8] C.U. Kim, J.C. Yu, E.D. Jung, I.Y. Choi, W. Park, H. Lee, I. Kim, D.-K. Lee, K.K. Hong, M.H. Song, K.J. Choi, Optimization of device design for low cost and high efficiency planar monolithic perovskite/silicon tandem solar cells, Nano Energy 60 (2019) 213–221.

[9] Z. Liu, J. Chang, Z. Lin, L. Zhou, Z. Yang, D. Chen, C. Zhang, S. (Frank) Liu, Y. Hao, High-performance planar perovskite solar cells using low temperature, solution-combustion-based nickel oxide hole transporting layer with efficiency exceeding 20%, Adv. Energy Mater. 8 (2018) 1703432.

[10] E. Aydin, J. Troughton, M. De Bastiani, E. Ugur, M. Sajjad, A. Alzahrani, M. Neophytou, U. Schwingenschlögl, F. Laquai, D. Baran, S. De Wolf, Room-temperature-sputtered nanocrystalline nickel oxide as hole transport layer for p–i–n perovskite solar cells, ACS Appl. Energy Mater. 1 (2018) 6227–6233.

[11] F. Ye, H. Chen, F. Xie, W. Tang, M. Yin, J. He, E. Bi, Y. Wang, X. Yang, L. Han, Soft-cover deposition of scaling-up uniform perovskite thin films for high cost-performance solar cells, Energy Environ. Sci. 9 (2016) 2295–2301.

[12] Z. Zhu, Y. Bai, T. Zhang, Z. Liu, X. Long, Z. Wei, Z. Wang, L. Zhang, J. Wang, F. Yan, S. Yang, High-performance hole-extraction layer of sol-gel-processed NiO nanocrystals for inverted planar perovskite solar cells, Angew. Chem. Int. Ed. 53 (2014) (n/a-n/a).

[13] H.L. Zhu, J. Cheng, D. Zhang, C. Liang, C.J. Reckmeier, H. Huang, A.L. Rogach, W.C.H. Choy, Room-temperature solution-processed NiO$_x$:PbI$_2$ nanocomposite structures for realizing high-performance perovskite photodetectors, ACS Nano 10 (2016) 6808–6815.

[14] J.H. Park, J. Seo, S. Park, S.S. Shin, Y.C. Kim, N.J. Jeon, H.-W. Shin, T.K. Ahn, J.H. Noh, S.C. Yoon, C.S. Hwang, S. Seok II, Seok, Efficient CH$_3$NH$_3$PbI$_3$ perovskite solar cells employing nanostructured p-type NiO electrode formed by a pulsed laser deposition, Adv. Mater. 27 (2015) 4013–4019.

[15] M.B. Islam, M. Yanagida, Y. Shirai, Y. Nabetani, K. Miyano, NiOx hole transport layer for perovskite solar cells with improved stability and reproducibility, ACS Omega 2 (2017) 2291–2299.

[16] M. Feng, M. Wang, H. Zhou, W. Li, X. Xie, S. Wang, Z. Zang, S. Chen, Optoelectronic modulation of undoped NiO$_x$ films for inverted perovskite solar cells via intrinsic defect regulation, ACS Appl. Energy Mater. 3 (2020) 9732–9741.

[17] V. Ganesh, B.R. Kumar, Y. Bitla, I.S. Yahia, S. AlFaify, Structural, optical and dielectric properties of Nd doped NiO thin films deposited with a spray pyrolysis method, J. Inorg. Organomet. Polym. Mater. 31 (2021) 2691–2699.

[18] R. Santbergen, R. Mishima, T. Meguro, M. Hino, H. Uzu, J. Blanker, K. Yamamoto, M. Zeman, Minimizing optical losses in monolithic perovskite/c-Si tandem solar cells with a flat top cell, Opt. Express 24 (2016) A1288.

[19] D. Zhang, M. Najafi, V. Zardetto, M. Dörenkämper, X. Zhou, S. Veenstra, L.J. Geerligs, T. Aernouts, R. Andriessen, High efficiency 4-terminal perovskite/c-Si tandem cells, Sol. Energy Mater. Sol. Cells 188 (2018) 1–5.

[20] L. Mazzarella, Y. Lin, S. Kirner, A.B. Morales-Vilches, L. Korte, S. Albrecht, E. Crossland, B. Stannowski, C. Case, H.J. Snaith, R. Schlatmann, Infrared light management using a nanocrystalline silicon oxide interlayer in monolithic perovskite/silicon heterojunction tandem solar cells with efficiency above 25%, Adv. Energy Mater. 9 (2019) 1803241.

[21] T. Cao, K. Chen, Q. Chen, Y. Zhou, N. Chen, Y. Li, Fullerene derivative-modified SnO$_2$ electron transport layer for highly efficient perovskite solar cells with efficiency over 21%, ACS Appl. Mater. Interfaces 11 (2019) 33825–33834.

[22] H. Yi, D. Wang, M.A. Mahmud, F. Haque, M.B. Upama, C. Xu, L. Duan, A. Uddin, Bilayer SnO$_2$ as electron transport layer for highly efficient perovskite solar cells, ACS Appl. Energy Mater. 1 (2018) 6027–6039.

[23] M. Hu, L. Zhang, S. She, J. Wu, X. Zhou, X. Li, D. Wang, J. Miao, G. Mi, H. Chen, Y. Tian, B. Xu, C. Cheng, Electron transporting bilayer of SnO$_2$ and TiO$_2$ nano-colloid enables highly efficient planar perovskite solar cells, Sol. RRL 4 (2020) 1900331.

[24] Y.W. Noh, I.S. Jin, K.S. Kim, S.H. Park, J.W. Jung, Reduced energy loss in SnO$_2$/ZnO bilayer electron transport layer-based perovskite solar cells for achieving high efficiencies in outdoor/indoor environments, J. Mater. Chem. A 8 (2020) 17163–17173.

[25] J. Ye, J. Li, A.A. Medjahed, S. Pouget, D. Aldakov, Y. Liu, P. Reiss, Doped bilayer tin (IV) oxide electron transport layer for high open-circuit voltage planar perovskite solar cells with reduced hysteresis, Small 17 (2021) 2005671.

[26] H.B. Lee, N. Kumar, M.M. Ovhal, Y.J. Kim, Y.M. Song, J. Kang, Dopant-free, amorphous–crystalline heterophase SnO$_2$ electron transport bilayer enables > 20% efficiency in triple-cation perovskite solar cells, Adv. Funct. Mater. 30 (2020) 2001559.

[27] J. Chung, S.S. Shin, K. Hwang, G. Kim, K.W. Kim, D.S. Lee, W. Kim, B.S. Ma, Y.-K. Kim, T.-S. Kim, J. Seo, Record-efficiency flexible perovskite solar cell and module enabled by a porous-planar structure as an electron transport layer, Energy Environ. Sci. 13 (2020) 4854–4861.

[28] Y. Guo, X. Yin, W. Que, NiO$_x$ mesoporous films derived from Ni(OH)$_2$ nanosheets for perovskite solar cells, J. Alloy. Compd. (2017) 839–845.

[29] S.S. Mali, H. Kim, H.H. Kim, S.E. Shim, C.K. Hong, Nanoporous p-type NiO$_x$ electrode for p-i-n inverted perovskite solar cell toward air stability, Mater. Today (2018) 483–500.

[30] Kai Yao, Fan Li, Qiqi He, Xiaofeng Wang, Yihua Jiang, Haitao Huang, Alex K.-Y. Jen, A copper-doped nickel oxide bilayer for enhancing efficiency and stability of hysteresis-free inverted mesoporous perovskite solar cells, Nano Energy (2017) 155–162.

[31] Y. Liu, J. Song, Y. Qin, Q. Qiu, Y. Zhao, L. Zhu, Y. Qiang, Cu-doped nickel oxide hole transporting layer via efficient low-temperature spraying combustion method for perovskite solar cells, J. Mater. Sci: Mater. Electron 31 (2019) 15627–15635.

[32] Guibin Shen, Xin Li, Yuqin Zou, Hongye Dong, Dongping Zhu, Yanglin Jiang, Xin Ren Ng, Fen Lin, Peter Müller-Buschbaum, Cheng Mu, High-performance and large-area inverted perovskite solar cells based on NiO$_x$ films enabled with a novel microstructure-control technology, Energy Environ. Mater. (2023) (12504).

[33] K.A. Bush, K. Frohna, R. Prasanna, R.E. Beal, T. Leijtens, S.A. Swifter, M.D. McGehee, Compositional engineering for efficient wide band gap perovskites with improved stability to photoinduced phase segregation, ACS Energy Lett. 3 (2018) 428–435.

[34] U. Kwon, B.G. Kim, D.C. Nguyen, J.H. Park, N.Y. Ha, S.J. Kim, S.H. Ko, S. Lee, D. Lee, H.J. Park, Solution-processible crystalline NiO nanoparticles for high-performance planar perovskite photovoltaic cells, Sci. Rep. 6 (2016) 1–10.

[35] Z.R. Marand, A. Kermanpur, F. Karimzadeh, E.M. Barea, E. Hassanabadi, E.H. Anaraki, B. Julián-López, S. Masi, I. Mora-Seró, Structural and electrical investigation of cobalt-doped NiOx/perovskite interface for efficient inverted solar cells, Nanomaterials 10 (2020) 872.

[36] P.-H. Lee, T.-T. Wu, C.-F. Li, D. Głowienka, Y.-H. Sun, Y.-T. Lin, H.-W. Yen, C.-G. Huang, Y. Galagan, Y.-C. Huang, W.-F. Su, Highly crystalline colloidal nickel oxide hole transport layer for low-temperature processable perovskite solar cell, Chem. Eng. J. 412 (2021) 128746.

[37] X. Xu, L. Li, F. Yu, H. Peng, X. Fang, X. Wang, Mesoporous high surface area NiO synthesized with soft templates: remarkable for catalytic CH4 deep oxidation, Mol. Catal. 441 (2017) 81–91.

[38] G. Bai, H. Dai, J. Deng, Y. Liu, K. Ji, Porous NiO nanoflowers and nanourchins: highly active catalysts for toluene combustion, Catal. Commun. 27 (2012) 148–153.

[39] W. Chen, F.Z. Liu, X.Y. Feng, A.B. Djurišić, W.K. Chan, Z.B. He, Cesium doped NiOx as an efficient hole extraction layer for inverted planar perovskite solar cells, Adv. Energy Mater. 7 (2017) 1–8.

[40] C.C. Boyd, R.C. Shallcross, T. Moot, R. Kerner, L. Bertoluzzi, A. Onno, S. Kavadiya, C. Chosy, E.J. Wolf, J. Werner, J.A. Raiford, C. de Paula, A.F. Palmstrom, Z.J. Yu, J.J. Berry, S.F. Bent, Z.C. Holman, J.M. Luther, E.L. Ratcliff, N.R. Armstrong, M.D. McGehee, Overcoming redox reactions at perovskite-nickel oxide interfaces to boost voltages in perovskite solar cells, Joule 4 (2020) 1759–1775.

[41] N. Kumar, H.B. Lee, R. Sahani, B. Tyagi, S. Cho, J.S. Lee, J.W. Kang, Room-temperature spray deposition of large-area SnO2 electron transport layer for high performance, stable FAPbI3-based perovskite solar cells, Small Methods 6 (2022) 1–12.

[42] B. Tyagi, H.B. Lee, N. Kumar, J.-W. Kang, Double-halide composition-engineered SnO2-triple cation perovskite solar cells demonstrating outstanding performance and stability, ACS Appl. Energy Mater. 3 (2020) 8595–8605.

[43] J. Sun, C. Shou, J. Sun, X. Wang, Z. Yang, Y. Chen, J. Wu, W. Yang, H. Long, Z. Ying, X. Yang, J. Sheng, B. Yan, J. Ye, NiOx-seeded self-assembled monolayers as highly hole-selective passivating contacts for efficient inverted perovskite solar cells, Sol. RRL 5 (2021) 2100663.

[44] J. Zhang, W. Mao, X. Hou, J. Duan, J. Zhou, S. Huang, W. Ou-Yang, X. Zhang, Z. Sun, X. Chen, Solution-processed Sr-doped NiOx as hole transport layer for efficient and stable perovskite solar cells, Sol. Energy 174 (2018) 1133–1141.

[45] Z. Jin, Y. Guo, S. Yuan, J.-S. Zhao, X.-M. Liang, Y. Qin, J.-P. Zhang, X.-C. Ai, Modification of NiOx hole transport layer for acceleration of charge extraction in inverted perovskite solar cells, RSC Adv. 10 (2020) 12289–12296.

[46] B. Tyagi, H.B. Lee, N. Kumar, W.-Y. Jin, K.-J. Ko, M.M. Ovhal, R. Sahani, H.-J. Chung, J. Seo, J.-W. Kang, High-performance, large-area semitransparent and tandem perovskite solar cells featuring highly scalable a-ITO/Ag mesh 3D top electrodes, Nano Energy 95 (2022) 106978.